Journal of Power Sources 327 (2016) 258–264

Contents lists available at ScienceDirect

Journal of Power Sources

journal homepage: www.elsevier.com/locate/jpowsour

# Performance enhancement of iron-chromium redox flow batteries by employing interdigitated flow fields

Y.K. Zeng [a], X.L. Zhou [a], L. Zeng [a, b], X.H. Yan [a], T.S. Zhao [a, *]

[a] *Department of Mechanical and Aerospace Engineering, The Hong Kong University of Science and Technology, Clear Water Bay, Kowloon, Hong Kong, China*
[b] *HKUST Jockey Club Institute for Advanced Study, The Hong Kong University of Science and Technology, Clear Water Bay, Kowloon, Hong Kong SAR, China*

## HIGHLIGHTS

- The ICRFBs with the interdigitated and serpentine flow fields are investigated.
- The IFF design enhances species transport in the porous electrode.
- The IFF design enables more uniform catalyst distribution in the porous electrode.
- The energy efficiency of the ICRFB with the IFF reaches 80.7% at 320 mA cm$^{-2}$.

## ARTICLE INFO

*Article history:*
Received 30 March 2016
Received in revised form
18 July 2016
Accepted 19 July 2016
Available online 25 July 2016

*Keywords:*
Flow batteries
Iron-chromium redox flow batteries
Interdigitated flow field
Mass transport
Energy storage

## ABSTRACT

The catalyst for the negative electrode of iron-chromium redox flow batteries (ICRFBs) is commonly prepared by adding a small amount of Bi$^{3+}$ ions in the electrolyte and synchronously electrodepositing metallic particles onto the electrode surface at the beginning of charge process. Achieving a uniform catalyst distribution in the porous electrode, which is closely related to the flow field design, is critically important to improve the ICRFB performance. In this work, the effects of flow field designs on catalyst electrodeposition and battery performance are investigated. It is found that compared to the serpentine flow field (SFF) design, the interdigitated flow field (IFF) forces the electrolyte through the porous electrode between the neighboring channels and enhances species transport during the processes of both the catalyst electrodeposition and iron/chromium redox reactions, thus enabling a more uniform catalyst distribution and higher mass transport limitation. It is further demonstrated that the energy efficiency of the ICRFB with the IFF reaches 80.7% at a high current density (320 mA cm$^{-2}$), which is 8.2% higher than that of the ICRFB with the SFF. With such a high performance and intrinsically low-cost active materials, the ICRFB with the IFF offers a great promise for large-scale energy storage.

## 1. Introduction

Deployment of intermittent renewable energy sources such as wind and solar energy has been increasing substantially, which raises an urgent demand to develop the large-scale energy storage devices for continuous and reliable power output [1–3]. The redox flow battery (RFB) has attracted extensive interests as a promising large-scale energy storage technology due to its unique advantages including ease of scalability, long cycle life, intrinsic safety and high efficiency [3]. In the past decades, various RFB systems have been proposed and developed [3–16]. However, the current RFB technologies still have not met the stringent cost and performance requirements for the broad penetration of energy storage market.

The iron-chromium redox flow battery (ICRFB) utilizes the low-cost and benign Fe(II)/Fe(III) and Cr(II)/Cr(III) redox couples in the acid supporting medium as the catholyte and anolyte, respectively [2,17]. The cost of chromium and iron active materials used in ICRFBs is estimated to be as low as \$17 kWh$^{-1}$, which provides the ICRFB a sufficient basis and great possibility to be a cost-effective energy storage system [2,17,18].

Historically, the ICRFB adopts a flow-through cell structure, in which the electrolyte is directly pumped through the porous electrode [19]. To bypass high pump loss, the conventional ICRFBs have thick electrodes (generally 3.0–6.0 mm) [20–22], leading to a high ohmic resistance [23,24]. For this reason, the conventional ICRFB is limited to a low operating current density of 80 mA cm$^{-2}$,

---

* Corresponding author.
*E-mail address:* metzhao@ust.hk (T.S. Zhao).

http://dx.doi.org/10.1016/j.jpowsour.2016.07.066
0378-7753/

resulting in bulky and costly cell stacks [18,25]. Recently, an ICRFB with the serpentine flow field (SFF) cell structure and carbon paper electrodes enables a high operating current density of 200 mA $cm^{-2}$, primarily due to a reduced ohmic loss [26].

In addition to the ohmic loss, the activation loss plays an important role in the battery performance, which is closely associated with the active surface area and electrochemical kinetics of redox couples. The Fe(II)/Fe(III) redox couple has an excellent electrochemical kinetics, and its kinetic constant is up to $8.6 \times 10^{-2}$ cm $s^{-1}$ on the oxidative pretreated pyrographite electrode [27]. The kinetics of the Cr(II)/Cr(III) redox couple is slow on most the carbonaceous electrodes, while the kinetic constant of Cr(II)/Cr(III) redox couple on the electrodeposited Bi catalyst is as high as $1.35 \times 10^{-3}$ cm $s^{-1}$ [28], which is generally comparable to other redox couples reported in the literature [29]. Moreover, the Bi catalyst has a high overpotential to suppress hydrogen evolution during the reducing process of Cr(III) to Cr(II). However, the Bi catalyst has a relatively low oxidation potential (0.05 V vs. SHE), and tends to be oxidized by air or ferric ions. To avoid this issue, the typical method for catalyst preparation is to add a small amount of $Bi^{3+}$ ions in the electrolyte and synchronously electrodeposit the metallic particles on the electrode at the beginning of charge process [1,25,30]. During the in-situ electrodeposition process, the flow field design has great influence on the mass transport and concentration distribution of $Bi^{3+}$ ions in the porous electrode, and further affects the catalyst distribution, which influences the active surface area and activation loss of the ICRFB. Previous studies have involved the effects of flow field designs on the mass transport characteristics in vanadium redox flow batteries (VRFBs) [22,31–34]. Shohji Tsushima *et al.* found that the VRFB with the interdigitated flow field (IFF) delivered a higher mass transport limitation than that with the SFF due to the enhanced convection of electrolyte in the electrodes [33]. In addition, other studies found that the IFF design has lower pump loss than the SFF design does [31,32].

Unlike the situations in VRFBs, the flow field designs in ICRFBs not only influence the transport and distribution of redox-active ions (Fe and Cr ions) in the porous electrode, but also affect the activation loss, as the Bi catalyst distribution is susceptible to the transport and concentration distribution of $Bi^{3+}$ ions (mM level) during the in-situ catalyst electrodeposition process. In this work, the effects of flow field designs on the catalyst electrodeposition process and battery performance are investigated. It is further found that the energy efficiency of the ICRFB with the IFF reaches 80.7% at a high operating current density of 320 mA $cm^{-2}$, which is 8.2% higher than that of the ICRFB with the SFF.

## 2. Experimental

### 2.1. ICRFB setup

The lab-scale ICRFB with the IFF was designed and fabricated. The carbon papers (SGL, 10AA, 0.4 mm thickness) were pretreated in air at 500 °C for 5 h and served as the electrodes. Both the negative and positive electrodes were made of two layers of carbon papers with active area of 2.0 cm × 2.0 cm, which were separated by the Nafion® NR-212 membrane. The polytetrafluoroethylene gaskets with 0.5 mm thickness were used to give an electrode compression ratio of approximately 40%. The IFFs with the channel depth 1.5 mm, the channel width 1.0 mm and rib width 1.0 mm were machined on the graphite plates. The gold-coated copper current collectors were adjacent to the graphite plates, and were clamped by the aluminum end plates. 20 mL mixed-reactant solutions of 1.0 M $FeCl_2$ (Aladdin) + 1.0 M $CrCl_3$ (Aladdin) + 3.0 M HCl (VWR) + 0.005 M $Bi^{3+}$ ($Bi_2O_3$: Aladdin) were used as both the anolyte and catholyte. The electrolytes were circulated in the Norprene® #16 Chemical Tubing by a 2-channel peristaltic pump (Longer pump, BT100-1F). The SFF design, one of the most widely used flow field design in fuel cells and flow batteries [9,31,35–39], was used for comparison. For the ICRFB with the SFF, the components such as the channel, rib, electrode, gasket and membrane were identical with the ICRFB with the IFF.

### 2.2. Test and characterization

The cell tests were conducted on Arbin BT2000 (Arbin® Instrument). The cell and the electrolyte reservoirs were placed in a temperature chamber at 65 °C. For the polarization test, the ICRFBs were charged to approximately 50% state-of-charge (SOC) before the tests. For each current density, the battery discharged for 20 s, rested for 10 s, and charged at the same current density for 20 s to keep the SOC constant during the polarization test. For the charge-discharge tests, the charge cut-off voltage was 1.2 V to mitigate hydrogen evolution, which could occur at the negative electrode during the charge process, and the discharge cut-off voltage was 0.8 V. The flow rate of the electrolyte was 50 mL $min^{-1}$. The cycle test was conducted at 320 mA $cm^{-2}$ and 65 °C, and 50 mL mixed-reactant solutions of 1.0 M $FeCl_2$ + 1.0 M $CrCl_3$ + 3.0 M

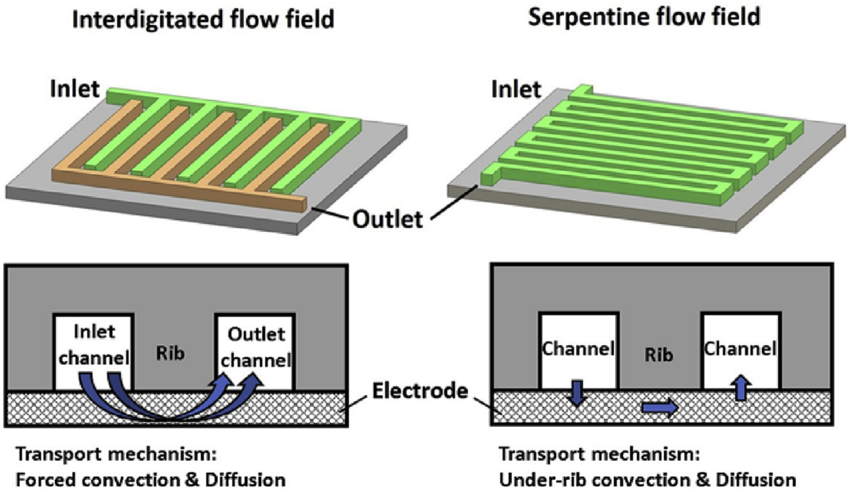

**Fig. 1.** Schematic of the interdigitated flow field and serpentine flow field.

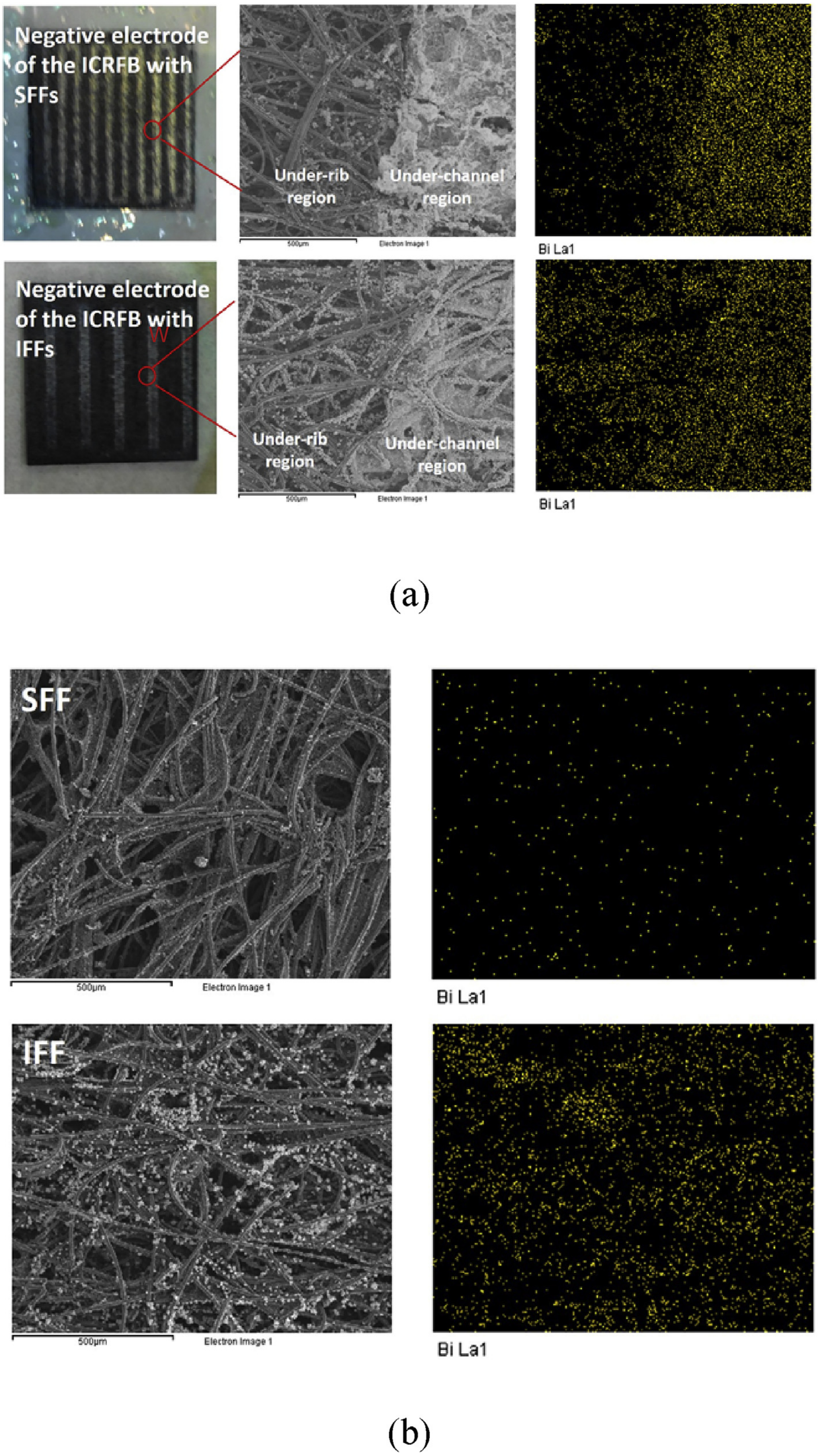

**Fig. 2.** SEM images and EDX mappings of (a) the electrodes near the current collector and (b) the electrode near the membrane in the ICRFBs with SFFs and IFFs.

HCl + 0.002 M $Bi^{3+}$ were used as both the anolyte and catholyte. The equivalent current density for feeding the initial electrolyte is 20.1 A $cm^{-2}$. The electrodes were characterized by a scanning electron microscope (JEOL-6300 SEM) and energy dispersive X-ray spectrum (EDX). The internal resistance of ICRFBs and electrochemical impedance spectroscopy (EIS) were measured by a

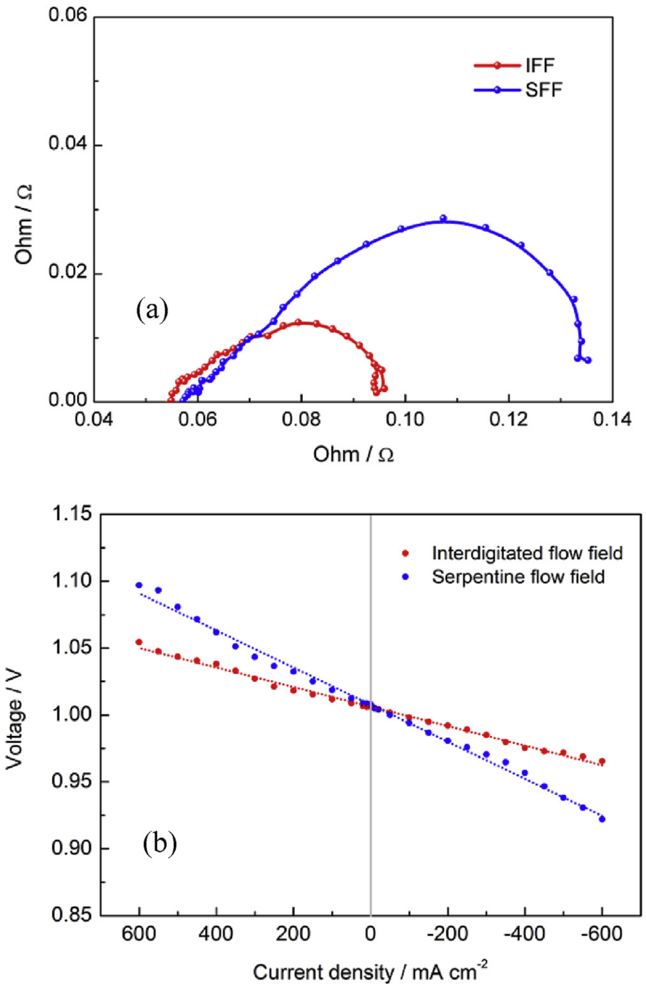

**Fig. 3.** (a) EIS and (b) IR-free polarization curves of the ICRFBs with IFFs and SFFs.

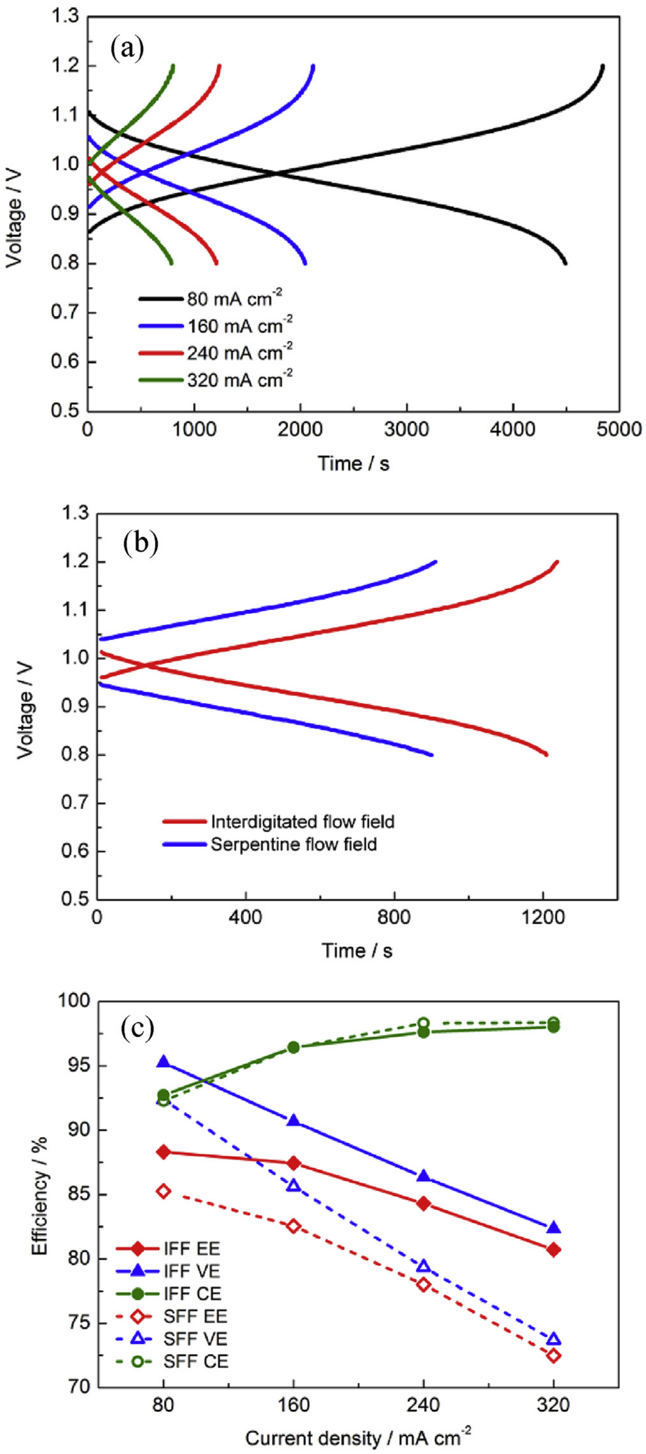

**Fig. 4.** (a) Charge-discharge curves of the ICRFB with IFFs at various current densities; (b) charge-discharge curves of the ICRFBs with IFFs and SFFs at 240 mA cm$^{-2}$; and (c) efficiencies of the ICRFBs with IFFs and SFFs.

potentiostat (EG&G Princeton, model M2273) with a frequency range from 100 kHz to 10 mHz.

## 3. Results and discussion

### 3.1. In-situ catalyst electrodeposition process

For the Cr(II)/Cr(III) redox reaction, catalysts such as Bi are needed to accelerate the reaction rate and simultaneously suppress the side reaction (hydrogen evolution). The Bi catalyst is electrodeposited on the negative electrode from Bi$^{3+}$ ions (5 mM) in the electrolyte with a current density of 20 mA cm$^{-2}$ at the beginning of charge process. The flow rate of 50 mL min$^{-1}$ initially provides a stoichiometric Bi$^{3+}$ flux of 301.6 mA cm$^{-2}$ (equivalent current density). The electrochemical reactions are as follows:

Positive electrode:

$$Fe^{2+} \xrightarrow{charge} Fe^{3+} + e^{-} \quad \mathrm{E}^0 = +0.77\ \mathrm{V\ vs.\ SHE} \tag{1}$$

Negative electrode:

$$Bi^{3+} + 3e^{-} \xrightarrow{charge} Bi \quad \mathrm{E}^0 = +0.05\ \mathrm{V\ vs.\ SHE} \tag{2}$$

After the catalyst electrodeposition, the Cr$^{3+}$ ions at the negative electrode are charged to Cr$^{2+}$ ions due to the lower redox potential (−0.41 V vs. SHE). If the catalyst is destroyed during the operation process of the ICRFB, it can be easily restored by totally stripping and then re-depositing [25].

The flow field serves to distribute active species across the entire electrode, which greatly impacts on the transport of Bi$^{3+}$ ions during the catalyst electrodeposition process. In the ICRFBs, the electrolytes are transported from the channels into the porous electrodes by convection and diffusion. Due to the low diffusivity and low concentration of Bi$^{3+}$ ions, the Bi$^{3+}$ ion flux driven by

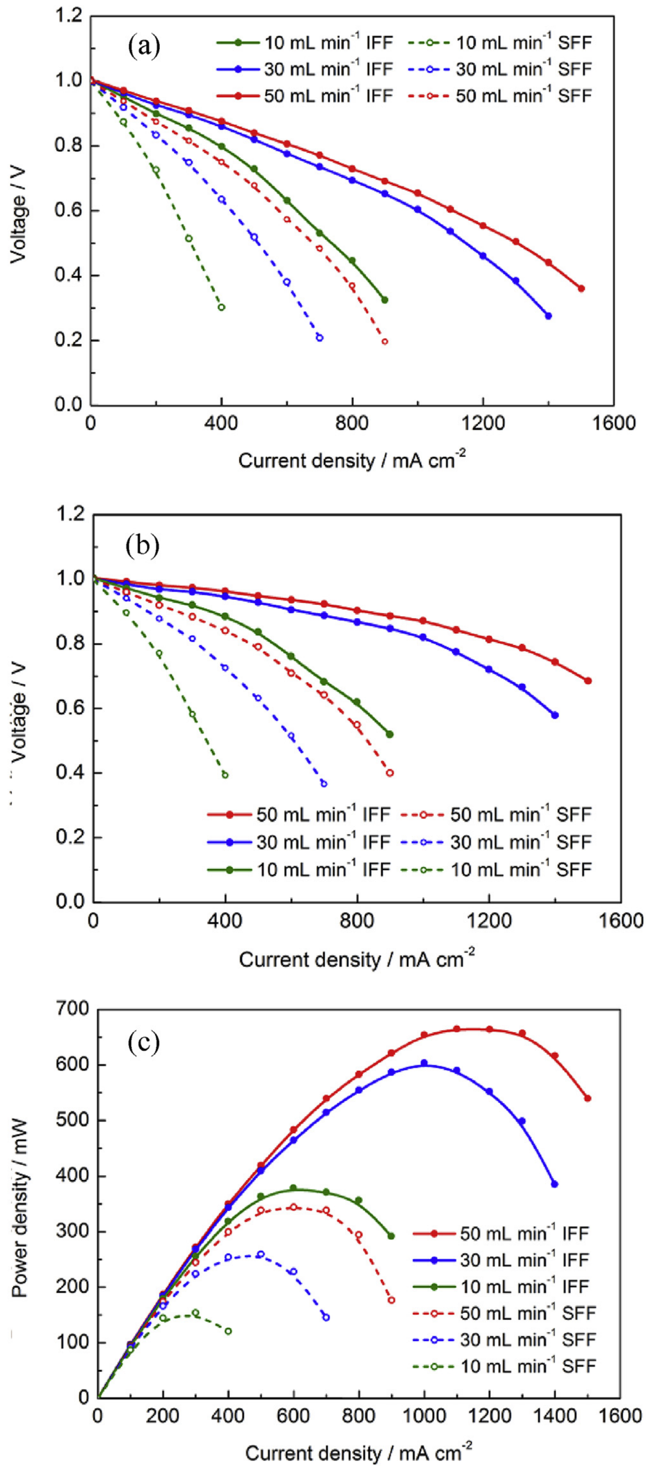

**Fig. 5.** (a) Discharge cell voltage, (b) IR-free discharge cell voltage and (c) output power density versus current density for the ICRFBs with IFFs and SFFs at various flow rates.

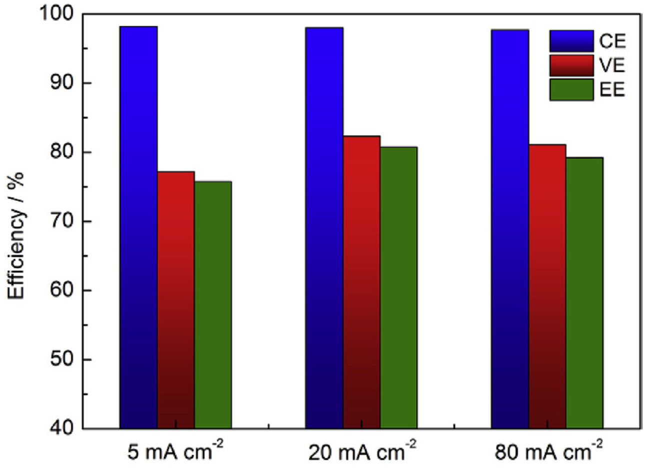

**Fig. 6.** The effect of the current density of catalyst electrodeposition on the battery performance.

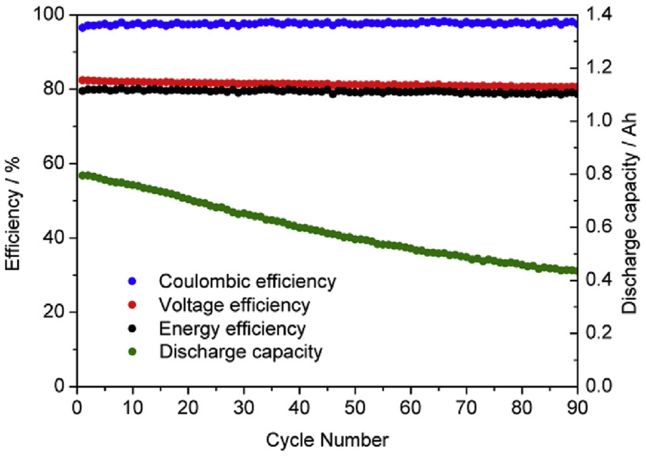

**Fig. 7.** Cycle performance of the ICRFB with IFFs at 320 mA cm$^{-2}$.

diffusion is quite limited. As shown in Fig. 1, the IFF design has non-continuous flow channels and forces all the electrolyte through the porous electrode between the neighboring inlet and outlet channels, thus providing strong forced convection. In the SFF design, the porous electrode hydraulically parallels to the flow field, and merely a portion of electrolyte flows through the porous electrode as the under-rib convection causing by the pressure drop between the two neighboring channels. Compared with the SFF design, the IFF design generally provides higher pressure drop between the two neighboring channels and stronger convective transport of species in the porous electrode [40].

As shown in Fig. 2a, the electrode near the current collector of the ICRFB with the IFF has a more uniform catalyst distribution from the under-channel to under-rib regions, characterized by SEM images and Bi element mappings. According to the EDX mappings of Fig. 2a, the bismuth amount of the IFF based ICRFB is significantly higher than that of the SFF based ICRFB at the under-rib region. The result indicates that the ICRFB with IFFs has better mass transport at the under-rib region of near-current-collector electrode compared to the ICRFB with SFFs. Fig. 2b shows the under-channel regions of the electrodes near the membrane. It is found that the ICRFB with the SFF has extremely low catalyst loading on the electrode near the membrane due to the limited mass transport. According to the element analysis by EDX mapping, the atomic ratio of Bi/C element is 1.006% for the near-membrane electrode of the ICRFB with the IFF, while it is merely 0.031% for that of the ICRFB with the SFF. Compared with the SFF design, the IFF design achieves higher catalyst loading at the electrode near the membrane, which is resulted by the stronger convection of the IFF design.

Fig. 3a shows the EIS of the ICRFBs with the IFF and SFF at the open-circuit condition (50% SOC). The internal resistance of the batteries are almost the same. The ICRFB with the IFF has significantly smaller semicircle compared with that with the SFF, which indicates the ICRFB with the IFF has smaller activation loss. This result is consistent with the IR-free charge-discharge polarization curve shown in Fig. 3b. At the region of low current densities that the mass transport loss is negligible, the ICRFB with the IFF shows smaller polarizations, indicating that the ICRFB with the IFF has smaller activation loss.

### 3.2. Charge-discharge performance

The charge-discharge performance of the ICRFB with the IFF is shown in Fig. 4a–b. The coulombic efficiencies of the two ICRFBs are almost identical. The voltage efficiency of the ICRFB with the IFF is 95.2% at 80 mA $cm^{-2}$, which is 2.8% higher than that of the ICRFB with the SFF (92.4%). The voltage efficiency of the ICRFB with the IFF still remains 86.4% at 240 mA $cm^{-2}$. As shown in Fig. 4b, at 240 mA $cm^{-2}$, the discharge curve of the ICRFB with the IFF is approximately 67 mV higher than that of the ICRFB with the SFF, while the charge curve of the ICRFB with the IFF is 79 mV lower than that of the ICRFB with the SFF. At a higher current density of 320 mA $cm^{-2}$, the energy efficiency of the ICRFB with the IFF is 80.7%, significantly higher than that of the ICRFB with the SFF (72.5%). Based on Figs. 3b and 5a–b, the polarization curves and IR-free polarization curves of both the IFF and SFF based ICRFBs at current densities of 80–320 mA $cm^{-2}$ are almost linear, which indicates that the mass transport loss is small within these current densities. Therefore, we infer that the dominant reason for the improved energy efficiency at 80–320 mA $cm^{-2}$ is the more uniform catalyst distribution. At the identical energy efficiency of approximately 80%, the operating current density of the ICRFB with the IFF dramatically increases from 200 to 320 mA $cm^{-2}$ compared to the ICRFB with the SFF. The higher current density means smaller cell stacks and lower cost for the same power requirement.

In addition to the more uniform distribution of Bi catalyst, the improved performance of the ICRFB with the IFF is also attributed to the enhanced mass transport of active species in the porous electrode, especially at high current densities (>600 mA $cm^{-2}$). According to the full-scale discharge polarization curves illustrated in Fig. 5a–b, the ICRFB with the IFF has remarkably higher performance compared to the ICRFB with the SFF, especially at high current densities. At the same flow rate, the influence of mass transport on the ICRFB with the IFF appears at higher current densities compared to the ICRFB with the SFF, indicating that the ICRFB with the IFF has smaller mass transport loss (higher mass transport limitation). As illustrated in Fig. 5c, the peak power density of the ICRFB with the IFF reaches 665 mW $cm^{-2}$ at 50 mL $min^{-1}$, 93% higher than that of the ICRFB with the SFF (344 mW $cm^{-2}$). With such a high power density, intrinsically low-cost active materials and non-precious Bi catalyst, the ICRFB with the IFF is expected to have strong competitiveness in the large-scale energy storage field.

The current density of catalyst electrodeposition should have influence on the catalyst electrodeposition and battery performance. The ICRFBs with the IFF have been tested at electrodeposition current densities of 5, 20 and 80 mA $cm^{-2}$. Then the charge-discharge tests are conducted at 320 mA $cm^{-2}$, and used to evaluate the battery performance [41]. As shown in Fig. 6, the ICRFB with 20 mA $cm^{-2}$ electrodeposition delivers the highest voltage efficiency as well as the highest energy efficiency. This is because that too high electrodeposition current density causes the uneven distribution of catalyst in the porous electrode. On the other hand, with the electrodeposition current density decreasing, the overpotential of the catalyst electrodeposition decreases, and the number of the activated nucleation sites for catalyst growth decreases, which leads to the larger catalyst particle size and smaller active catalytic surface [42].

### 3.3. Cycle performance

The stability of ICRFBs is of great significance for the practical application. It is desirable that the battery can work stably and have a small capacity decay rate. The cycle test is conducted at 320 mA $cm^{-2}$ and 65 °C with the voltage window of 0.8–1.2 V. The 50 mL electrolytes with a theoretical capacity of 1.34 Ah are used as both positive and negative electrolytes. As presented in Fig. 7, the voltage efficiency, coulombic efficiency and energy efficiency of the ICRFB with the IFF are stable. The capacity decay rate is 0.5% per cycle, significantly lower than that of the reported ICRFB [18]. The decayed capacity can be recovered by the rebalancing process [25].

## 4. Conclusions

In summary, the effects of the flow field design on the catalyst electrodeposition and battery performance are investigated, and characterized by the SEM image and EDX mapping, EIS, polarization curve, charge-discharge curve. With the forced convection of electrolyte in the porous electrode, the IFF design enhances transport of $Bi^{3+}$ in the porous electrode during the catalyst electrodeposition, enables a more uniform catalyst distribution, and reduces the activation loss compared with the SFF design. Moreover, the ICRFB with the IFF exhibits higher mass transport limitation. It is demonstrated that the ICRFB with the IFF achieves a high current density of 320 mA $cm^{-2}$ with the energy efficiency above 80%, which renders the ICRFB outstanding competitiveness for large-scale energy storage.

## Acknowledgements

The work described in this paper was fully supported by a grant from the Research Grants Council of the Hong Kong Special Administrative Region, China (Project No. 623313).

## References

[1] B. Li, M. Gu, Z. Nie, Y. Shao, Q. Luo, X. Wei, X. Li, J. Xiao, C. Wang, V. Sprenkle, Bismuth nanoparticle decorating graphite felt as a high-performance electrode for an all-vanadium redox flow battery, Nano Lett. 13 (2013) 1330–1335.

[2] W. Wang, Q. Luo, B. Li, X. Wei, L. Li, Z. Yang, Recent progress in redox flow battery research and development, Adv. Funct. Mater. 23 (2013) 970–986.

[3] Z. Yang, J. Zhang, M.C. Kintner-Meyer, X. Lu, D. Choi, J.P. Lemmon, J. Liu, Electrochemical energy storage for green grid, Chem. Rev. 111 (2011) 3577–3613.

[4] B. Huskinson, M.P. Marshak, C. Suh, S. Er, M.R. Gerhardt, C.J. Galvin, X. Chen, A. Aspuru-Guzik, R.G. Gordon, M.J. Aziz, A metal-free organic-inorganic aqueous flow battery, Nature 505 (2014) 195–198.

[5] K.L. Hawthorne, J.S. Wainright, R.F. Savinell, Studies of iron-ligand complexes for an all-iron flow battery application, J. Electrochem. Soc. 161 (2014) A1662–A1671.

[6] M.C. Wu, M.Y. Liu, G.F. Long, K. Wan, Z.X. Liang, T.S. Zhao, A novel high-energy-density positive electrolyte with multiple redox couples for redox flow batteries, Appl. Energy 136 (2014) 576–581.

[7] K. Gong, X. Ma, K.M. Conforti, K.J. Kuttler, J.B. Grunewald, K.L. Yeager, M.Z. Bazant, S. Gu, Y. Yan, A zinc–iron redox-flow battery under $100 per kw h of system capital cost, Energy Environ. Sci. 8 (2015) 2941–2945.

[8] M.C. Tucker, K.T. Cho, A.Z. Weber, Optimization of the iron-ion/hydrogen redox flow cell with iron chloride catholyte salt, J. Power Sources 245 (2014) 691–697.

[9] K. Lin, Q. Chen, M.R. Gerhardt, L. Tong, S.B. Kim, L. Eisenach, A.W. Valle, D. Hardee, R.G. Gordon, M.J. Aziz, Alkaline quinone flow battery, Science 349 (2015) 1529–1532.

[10] X.L. Zhou, T.S. Zhao, L. An, Y.K. Zeng, X.H. Yan, A vanadium redox flow battery model incorporating the effect of ion concentrations on ion mobility, Appl. Energy 158 (2015) 157–166.

[11] X.L. Zhou, T.S. Zhao, L. An, L. Wei, C. Zhang, The use of polybenzimidazole membranes in vanadium redox flow batteries leading to increased coulombic efficiency and cycling performance, Electrochim. Acta 153 (2015) 492–498.

[12] X.L. Zhou, Y.K. Zeng, X.B. Zhu, L. Wei, T.S. Zhao, A high-performance dual-scale porous electrode for vanadium redox flow batteries, J. Power Sources 325 (2016) 329–336.

[13] L. Wei, T.S. Zhao, G. Zhao, L. An, L. Zeng, A high-performance carbon nanoparticle-decorated graphite felt electrode for vanadium redox flow batteries, Appl. Energy 176 (2016) 74–79.

[14] L. Wei, T.S. Zhao, L. Zeng, X.L. Zhou, Y.K. Zeng, Titanium carbide nanoparticle-decorated electrode enables significant enhancement in performance of all-vanadium redox flow batteries, Energy Technol. (2016), http://dx.doi.org/10.1002/ente.201600016.

[15] Q. Liu, G. Grim, A. Papandrew, A. Turhan, T.A. Zawodzinski, M.M. Mench, High performance vanadium redox flow batteries with optimized electrode configuration and membrane selection, J. Electrochem. Soc. 159 (2012) A1246–A1252.

[16] P. Leung, J. Palma, E. Garcia-Quismondo, L. Sanz, M. Mohamed, M. Anderson, Evaluation of electrode materials for all-copper hybrid flow batteries, J. Power Sources 310 (2016) 1–11.

[17] L.H. Thaller, Electrically Rechargeable Redox Flow Cells, NASA TM X-71540, Lewis Research Centre, 1974.

[18] Y.K. Zeng, T.S. Zhao, L. An, X.L. Zhou, L. Wei, A comparative study of all-vanadium and iron-chromium redox flow batteries for large-scale energy storage, J. Power Sources 300 (2015) 438–443.

[19] L.H. Thaller, Recent Advances in Redox Flow Cell Storage Systems, NASA TM-79186, Lewis Research Centre, 1979.

[20] Q. Ye, J. Hu, P. Cheng, Z. Ma, Design trade-offs among shunt current, pumping loss and compactness in the piping system of a multi-stack vanadium flow battery, J. Power Sources 296 (2015) 352–364.

[21] N. Hagedorn, M. Hoberecht, L. Thaller, Nasa-redox Cell-stack Shunt Current, Pumping Power, and Cell-performance Tradeoffs, National Aeronautics and Space Administration, Cleveland, OH (USA), 1982. Lewis Research Center.

[22] R.M. Darling, M.L. Perry, The influence of electrode and channel configurations on flow battery performance, J. Electrochem. Soc. 161 (2014) A1381–A1387.

[23] M. Lopez-Atalaya, G. Codina, J. Perez, J. Vazquez, A. Aldaz, Optimization studies on a Fe/Cr redox flow battery, J. Power Sources 39 (1992) 147–154.

[24] R.F. Gahn, J. Charleston, J.S. Ling, M.A. Reid, Performance of Advanced Chromium Electrodes for the NASA Redox Energy Storage System, National Aeronautics and Space Administration, Cleveland, OH (USA), 1981. Lewis Research Center.

[25] R.F. Gahn, N.H. Hagedorn, J.A. Johnson, Cycling Performance of the Iron-Chromium Redox Energy Storage System, NASA TM-87034, Lewis Research Centre, 1985.

[26] Y.K. Zeng, X.L. Zhou, L. An, L. Wei, T.S. Zhao, A high-performance flow-field structured iron-chromium redox flow battery, J. Power Sources 324 (2016) 738–744.

[27] E. Hollax, D.S. Cheng, The influence of oxidative pretreatment of graphite electrodes on the catalysis of the Cr3+/Cr2+ and Fe3+/Fe2+ redox reactions, Carbon 23 (1985) 655–664.

[28] C. Wu, D. Scherson, E. Calvo, E. Yeager, M. Reid, A bismuth-based electrocatalyst for the chromous-chromic couple in acid electrolytes, J. Electrochem. Soc. 133 (1986) 2109–2112.

[29] C. Ding, H. Zhang, X. Li, T. Liu, F. Xing, Vanadium flow battery for energy storage: prospects and challenges, J. Phys. Chem. Lett. 4 (2013) 1281–1294.

[30] R.F. Gahn, N.H. Hagedorn, J.S. Ling, Single Cell Performance Studies on the Fe/Cr Redox Energy Storage System Using Mixed Reactant Solutions at Elevated Temperature, NASA TM-83385, Lewis Research Centre, 1983.

[31] C. Dennison, E. Agar, B. Akuzum, E. Kumbur, Enhancing mass transport in redox flow batteries by tailoring flow field and electrode design, J. Electrochem. Soc. 163 (2016) A5163–A5169.

[32] J. Houser, J. Clement, A. Pezeshki, M.M. Mench, Influence of architecture and material properties on vanadium redox flow battery performance, J. Power Sources 302 (2016) 369–377.

[33] S. Tsushima, S. Sasaki, S. Hirai, in: Proceedings of ECS Meeting, San Francisco, 2013, 1664–1664.

[34] Q. Xu, T.S. Zhao, P.K. Leung, Numerical investigations of flow field designs for vanadium redox flow batteries, Appl. Energy 105 (2013) 47–56.

[35] D. Aaron, Q. Liu, Z. Tang, G. Grim, A. Papandrew, A. Turhan, T. Zawodzinski, M. Mench, Dramatic performance gains in vanadium redox flow batteries through modified cell architecture, J. Power Sources 206 (2012) 450–453.

[36] Q. Xu, T.S. Zhao, C. Zhang, Performance of a vanadium redox flow battery with and without flow fields, Electrochim. Acta 142 (2014) 61–67.

[37] L. An, T.S. Zhao, X.L. Zhou, X.H. Yan, C.Y. Jung, A low-cost, high-performance zinc–hydrogen peroxide fuel cell, J. Power Sources 275 (2015) 831–834.

[38] A.M. Pezeshki, J.T. Clement, G.M. Veith, T.A. Zawodzinski, M.M. Mench, High performance electrodes in vanadium redox flow batteries through oxygen-enriched thermal activation, J. Power Sources 294 (2015) 333–338.

[39] Y.K. Zeng, P. Fan, X. Zhang, C. Fu, J. Li, G. Li, Sensitivity analysis for a planar sofc: size effects of the porous gas diffusion layer underneath the channel rib, Fuel Cells 14 (2014) 123–134.

[40] T.J. Latha, S. Jayanti, Hydrodynamic analysis of flow fields for redox flow battery applications, J. Appl. Electrochem. 44 (2014) 995–1006.

[41] Q. Zheng, F. Xing, X. Li, T. Liu, Q. Lai, G. Ning, H. Zhang, Investigation on the performance evaluation method of flow batteries, J. Power Sources 266 (2014) 145–149.

[42] V. Richoux, S. Diliberto, C. Boulanger, J. Lecuire, Pulsed electrodeposition of bismuth telluride films: influence of pulse parameters over nucleation and morphology, Electrochim. Acta 52 (2007) 3053–3060.